

# Modeling combined coherent and incoherent scattering structures for light trapping in solar cells

Aimi Abass,<sup>1,a)</sup> Christos Trompoukis,<sup>2,3</sup> Sven Leyre,<sup>3,4</sup> Marc Burgelman,<sup>1</sup> and Bjorn Maes<sup>5,6</sup>

<sup>1</sup>*Ghent University, Electronics and Information Systems (ELIS), Sint-Pietersnieuwstraat 41, B-9000 Gent, Belgium*

<sup>2</sup>*IMEC, Kapeldreef 75, B-3001 Leuven, Belgium*

<sup>3</sup>*ESAT/ELECTA, KU Leuven, Kasteelpark Arenberg 10, B-3001 Leuven, Belgium*

<sup>4</sup>*Light & Lighting Laboratory, Catholic University College Ghent, Gebroeders Desmetstraat 1, B-9000 Gent, Belgium*

<sup>5</sup>*Micro- and Nanophotonic Materials Group, Faculty of Science, University of Mons, B-7000 Mons, Belgium*

<sup>6</sup>*Photonics Research Group, Department of Information Technology, Ghent University-IMEC, Sint-Pietersnieuwstraat 41, B-9000 Gent, Belgium*

(Received 22 April 2013; accepted 18 June 2013; published online 15 July 2013)

Current structures for solar cells or LEDs often incorporate layers of various optical regimes, with a mixture of coherent, partially coherent or incoherent behavior. We developed a simple and efficient calculation method to study such combined solar cell structures with both wave and ray optics sections. These One-Pass Coherent calculations take wave effects into account where they matter the most, while avoiding a large computational domain to model rough structures. The method simulates a general diffuser by working directly with the reflected wavefronts, instead of using its geometry. We utilize this method to study thin film silicon solar cell structures with a grating on the front and a diffuser at the back. More absorption is obtained with the combined light trapping scheme of appropriate characteristics, compared with grating-only or diffuser-only counterparts. Finally, we report a significant effect of incoherence on the absorption of fairly thin ( $\sim 10 \mu\text{m}$ ) cells. We demonstrate that partially incoherent light can be more efficiently absorbed than fully coherent light on average over a broad wavelength range. It turns out that the scarcity of guided modes for fully coherent light can hinder the grating enhancement, leading to a consistently better performance when light coherence is limited or lost. © 2013 AIP Publishing LLC.

[<http://dx.doi.org/10.1063/1.4813102>]

## I. INTRODUCTION

The development of thin film solar cell technologies spurs much research work on light trapping techniques to make them competitive with preexisting solar technologies. Various nanostructures, whether periodically structured or random, have been proposed to fit the material choices for thin film cells.<sup>1–12</sup> It was shown that the absorption enhancement from periodic grating structures can exceed the Lambertian limit in the case of thin film cells of a few wavelengths thick or smaller.<sup>13–15</sup> Spinelli *et al.* have recently shown that a nanopatterned Si surface can suppress reflection to below 3% throughout the wavelength range of 450–900 nm.<sup>16</sup> For thin film cells with thickness in the range larger than a few wavelengths, random light trapping structures were shown to give comparable or larger enhancement compared with periodic structures.<sup>3,13</sup>

As most of the proposed grating structures tend to function optimally in a limited wavelength range, the combination of different structures was considered. Much research was done on dual interface grating structures, which have front and back gratings in a single solar cell structure.<sup>17–20</sup> We previously demonstrated that the two gratings can complement each other in enabling access to different photonic phenomena.<sup>18</sup> Martins *et al.* showed how superposing

gratings with different phases at one interface can lead to more absorption enhancement, by increasing higher order diffraction while suppressing the lower order processes.<sup>21</sup> These supercell gratings can be interpreted as a compromise between rough diffusers and periodic grating structures, due to the length of one supercell period and the resulting complex geometry. Such structures partially combine the benefits of periodicity and roughness, balancing the amount of available diffraction orders with their relative diffraction efficiencies.

Here, we study light trapping by rough diffusers and gratings, by having each at a different interface. More specifically, we examine combined structures with gratings at the front and rough diffusers at the back for thin film Si solar cells. The grating structures on the front provide flexibility in tailoring anti-reflection properties and light coupling. The diffuser at the back will mainly serve to increase the optical path length. This combined front-grating-back-diffuser structure couples the regimes of wave and ray optics.

The combined structures provide several computational challenges. On the one hand, wavelength scale gratings require one to take into account coherent effects. On the other hand, calculating a rough diffuser in a full wave simulation would typically require a huge computational domain. Furthermore, it is of great interest to simulate these combined structures in the thickness regime beyond several wavelengths and thus beyond the coherence length of

<sup>a)</sup>Electronic mail: [aimi.abass@elis.ugent.be](mailto:aimi.abass@elis.ugent.be)

sunlight. To address these complications, a simulation technique is developed, which circumvents the need to fully implement an extensive disordered geometry while taking into account coherent effects where they matter. With our approach, we can efficiently model 2D or 3D devices combining coherent and incoherent features, which is impossible with the reported 1D methods.<sup>22–26</sup> A full wave simulation method that can take into account partially coherent light by considering the Fourier components of the time signal has been described.<sup>27</sup> However, it still faces the same obstacles as other standard wave simulation techniques when used to simulate random diffusing structures.

In Sec. II of the paper, we describe the developed calculation method. Section III provides basic examples of calculation results. In Sec. IV, we report the, perhaps, unexpected beneficial effect of incoherence for a particular range of Si thicknesses. It is found that partially coherent light can be absorbed more than fully coherent light on average throughout a wide wavelength range when certain conditions of the cell geometry are fulfilled. In Sec. V, we examine more complex combined devices, exploring the effects of specular reflection by the back diffuser, active material thickness, and the front grating periodicity.

## II. CALCULATION METHOD

As mentioned in Sec. I, there is a dilemma in simulating a combined diffuser and grating structure as in Fig. 1(a): Ray

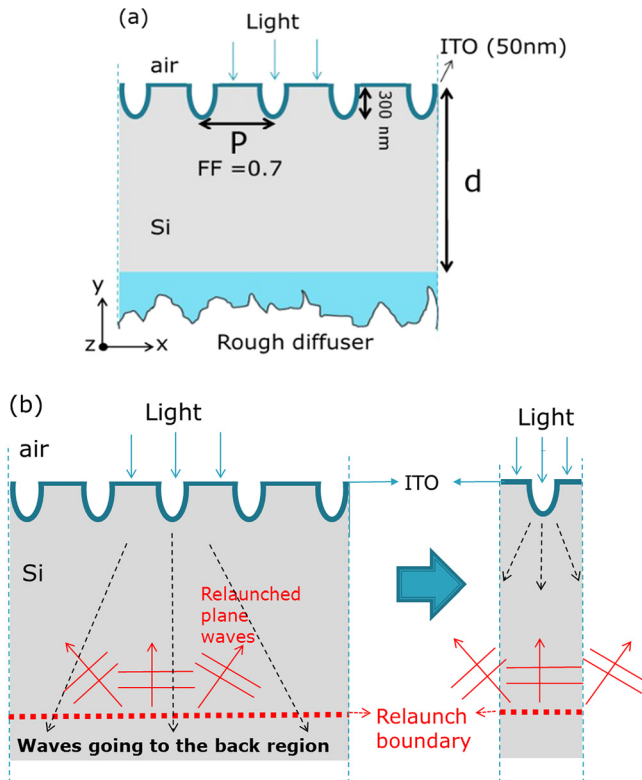


FIG. 1. (a) The system under consideration.  $P$  is the grating period,  $FF$  is the grating fill factor, and  $d$  is the thickness of the Si layer. The horizontal diameter of the grating feature is  $P \times FF$ . The front part is coated with an ITO layer of 50 nm thickness. (b) The proposed computational method which replaces the rough diffuser structure with a computational boundary and reduces the simulation domain to a single period of the grating.

optics is not accurate enough, whereas full wave simulation is computationally costly. This problem is circumvented by directly considering the wavefront reflected by the diffuser, instead of its rough geometry, which can be represented as a superposition of plane waves with a certain spatial frequency spectrum.<sup>28,29</sup> We propose to model the back diffuser with a computational boundary which passes through incoming waves (towards  $-y$ ) and relaunched plane waves with various directions (towards  $+y$ ) into the structure (Fig. 1(b)). The relaunched plane waves are determined in such a way that together they model the wavefront that comes out from the diffuser or any other selected structure at the bottom.

The details of the computational steps are shown in Fig. 2. One first calculates the coherent field profile resulting from each relevant incident plane wave on the structure with the front grating (Fig. 2(a)): one solar excitation direction from the front (air-side) as the “first pass” field profile (for each wavelength), and multiple (relaunched) directions from the back (Si-side). If we consider the incoming sunlight to be fully coherent or if the thickness of the cell structure is smaller than the coherence length, we would have to calculate the coherent superposition of these calculated fields and know the phase relation between incoming and relaunched plane waves. However, if we can consider that coherence is broken after the bottom diffuser, the calculations of the total system response (absorption  $A_{tot}(\lambda)$ , reflectance  $R_{tot}(\lambda)$  and transmittance  $T_{tot}(\lambda)$ ) are simplified. Then, we only need to consider interference effects for each launched plane wave separately and locally when it interacts with the front grating structure, and not between launched plane waves. By taking this assumption, the plane waves are treated as if they have their coherent length limited to the path length in one pass through the structure. Therefore, we refer to this method as One-Pass Coherent (OPC) calculations. The “loss of coherence” is applicable when the active material thickness itself is larger than the coherence length of light, or when the bottom diffusing structure is a bulk diffuser which makes light travel and scatter over a relatively long distance before coming back to the active material. One can therefore model any kind of bottom diffuser by calculating only one period of the front grating (Fig. 1(b)). In essence, we trade complexity in real space for complexity in  $k$ -space. This method can treat any kind of structure at the bottom as long as the OPC assumption is valid and the reflected wavefront information is known.

Various “one pass” quantities necessary to calculate the total system response are obtained from the plane wave field profiles (Fig. 2(a)). From the first pass field profile (incident sunlight), we determine the first pass absorption ( $A_{first}(\lambda)$ ), reflectance ( $R_{first}(\lambda)$ ), and transmittance ( $T_{first}(k_{||}', \lambda)$ , details below). Subsequently, from the field profiles of the relaunched plane waves, the one pass relaunch absorption ( $A_{k_{||}}(\lambda)$ ), escape transmittance ( $R_{k_{||}}(\lambda)$ ), and relaunch reflectance ( $T_{k_{||}}(k_{||}', \lambda)$ ) are extracted for every possible transverse excitation propagation constant  $k_{||} \leq k_{Si}$ . Here,  $k_{Si} = k \times n_{Si}$  where  $k$  is the propagation constant in air and  $n_{Si}$  is the refractive index of silicon. The subscripts  $k_{||}$  indicate the transverse direction ( $x$ - or  $z$ -axis in Fig. 1(a)) of the plane wave excitation. The arguments  $k_{||}'$  indicate the transverse plane

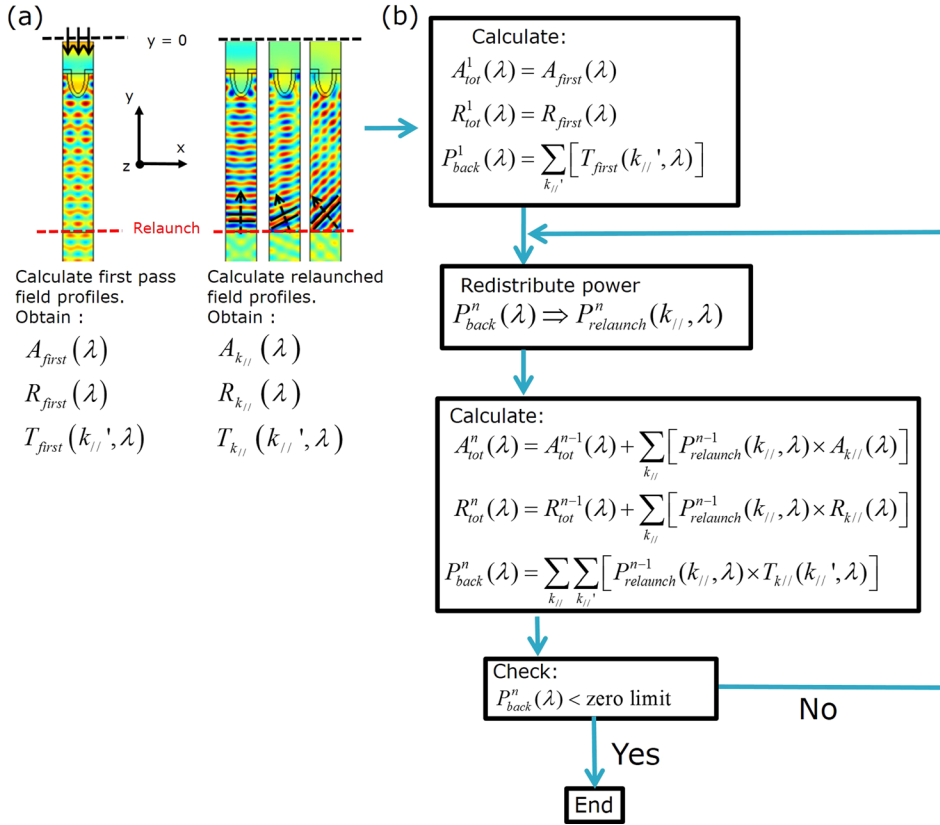


FIG. 2. Computational scheme assuming a lossless back diffuser or reflector. (a) One pass field profile calculations. (b) OPC iteration.

wave component of the response in that particular direction. Note that the  $R_{first}(\lambda)$  and  $R_{k_{||}}(\lambda)$  always indicate power escaping from the solar structure to air (towards  $+y$ ).  $T_{first}(k_{||}', \lambda)$  and  $T_{k_{||}}(k_{||}', \lambda)$  always indicate power fractions going to the bottom of the cell (towards  $-y$ ).

We provide now more details on how these quantities are determined. For clarity, we describe the calculations only for 2D systems invariant along the  $z$ -axis and assume that the launched power for each plane wave is already normalized over one cell of the grating. The one pass absorption is calculated via the divergence of the poynting vector over the absorbing volume (area in 2D)

$$A_q(\lambda) = \int (\nabla \cdot \vec{S}_q(\lambda)) dV, \quad (1)$$

where  $\vec{S}_q(\lambda)$  is the poynting vector defined as

$$\vec{S}_q(\lambda) = \frac{1}{2} \text{Re}[\vec{E}_q(\lambda) \times \vec{H}_q(\lambda)^*], \quad (2)$$

where  $\vec{E}_q$  is the electric field and  $\vec{H}_q$  is the magnetic field. The subscript  $q$  indicates whether it is the first pass case or a certain  $k_{||}$  relaunch case.  $R_{first}(\lambda)$  and  $R_{k_{||}}(\lambda)$  to air are obtained via

$$R_{first}(\lambda) = \int_{\text{P}} (\vec{S}_{first}^{scat}(\lambda) \cdot \vec{j}) dx \Big|_{y=0}, \quad (3)$$

$$R_{k_{||}}(\lambda) = \int_{\text{P}} (\vec{S}_{k_{||}}(\lambda) \cdot \vec{j}) dx \Big|_{y=0}, \quad (4)$$

calculated above the grating structure as shown in Fig. 2(a) along one period  $P$ .  $\vec{S}_{first}^{scat}(\lambda)$  refers to the scattered wave poynting vector for the first launch case and  $\vec{j}$  is the unit vector in the  $y$  direction. The scattered field can be obtained using the relation:

$$\psi^{scat} = \psi - \psi^{incidence}, \quad (5)$$

where  $\psi$  is the total electric or magnetic field and  $\psi^{incidence}$  is the incident plane wave.

For our method, it is necessary to decompose the scattered wave towards the bottom into a set of plane waves. One can use this information to consider specular reflection by relaunching plane waves with the same amplitude and  $k_{||}$ . We obtain these components via Fourier decomposition along the relaunch boundary:

$$\tilde{\psi}_{k_{||}'}|_{relaunch} = \left( \frac{1}{P} \right) \int_{\text{P}} \psi(x) e^{-ik_{||}'x} dx, \quad (6)$$

where  $\tilde{\psi}_{k_{||}'}$  is the amplitude of a Fourier component of the electric or magnetic field. With these Fourier components, we calculate  $T_{first}(k_{||}', \lambda)$  and  $T_{k_{||}}(k_{||}', \lambda)$  which are the portions of the total power carried by each component to the bottom:

$$T_{first}(k_{||}', \lambda) = \int_{\text{P}} (-\vec{S}_{first, k_{||}'}^{scat}(\lambda) \cdot \vec{j}) dx \Big|_{relaunch}, \quad (7)$$

$$T_{k_{||}}(k_{||}', \lambda) = \int_{\text{P}} (-\vec{S}_{k_{||}, k_{||}'}^{scat}(\lambda) \cdot \vec{j}) dx \Big|_{relaunch}, \quad (8)$$

which are calculated along the relaunch boundary in one grating period with

$$\vec{S}_{k_{\parallel},k_{\parallel}'}^{scat}(\lambda) = \frac{1}{2} \text{Re}[\vec{E}_{k_{\parallel},k_{\parallel}'}^{scat}(\lambda) \times \vec{H}_{k_{\parallel},k_{\parallel}'}^{scat}(\lambda)^*], \quad (9)$$

where  $\vec{\psi}_{k_{\parallel},k_{\parallel}'}^{scat}(\lambda)$  is the scattered  $k_{\parallel}'$  Fourier component for a  $k_{\parallel}$  plane wave excitation (here,  $\vec{\psi}$  represents  $\vec{S}$ ,  $\vec{E}$ , or  $\vec{H}$ ).

Now, we have enough information to start the subsequent OPC iteration procedure for the bottom structure (Fig. 2(b)). Note that to model any kind of reflector at the bottom for a particular top grating, we only need to calculate the previous quantities once. With these values, we proceed to take into account the reflector, which can have both diffuse and specular components. Here, it is assumed that the back reflector/diffuser is lossless and thus  $T_{tot}(\lambda) = 0$ . To obtain the total system response ( $A_{tot}(\lambda)$  and  $R_{tot}(\lambda)$ ), we start from the first response ( $A_{first}(\lambda)$ ,  $R_{first}(\lambda)$  and  $T_{first}(k_{\parallel}', \lambda)$ ) and iteratively add the contributions of relaunched waves, until the power to be relaunched from the back side is close to zero (Fig. 2(b)). Utilizing the fact there is no coherent interaction between different plane wave launches, the total response is calculated with

$$A_{tot}^n(\lambda) = A_{tot}^{n-1}(\lambda) + \sum_{k_{\parallel}} [P_{relaunch}^{n-1}(k_{\parallel}, \lambda) \times A_{k_{\parallel}}(\lambda)], \quad (10)$$

$$R_{tot}^n(\lambda) = R_{tot}^{n-1}(\lambda) + \sum_{k_{\parallel}} [P_{relaunch}^{n-1}(k_{\parallel}, \lambda) \times R_{k_{\parallel}}(\lambda)], \quad (11)$$

where  $P_{relaunch}^n(k_{\parallel}, \lambda)$  is the relaunched power distribution (explained below). We can account for a lossy back reflector/diffuser without much added difficulty by relaunching the power that passes the relaunch boundary only partially. The values at the first iteration are determined from the first pass responses,

$$A_{tot}^1(\lambda) = A_{first}(\lambda), \quad (12)$$

$$R_{tot}^1(\lambda) = R_{first}(\lambda). \quad (13)$$

At every iteration, the relaunched power distribution  $P_{relaunch}^n(k_{\parallel}, \lambda)$  (towards +y) consists of specular and diffuse components

$$P_{relaunch}^n(k_{\parallel}, \lambda) = \Phi_{Dif}^n(k_{\parallel}, \lambda) + \Phi_{Spec}^n(k_{\parallel}, \lambda), \quad (14)$$

where  $\Phi_{Dif}^n(k_{\parallel}, \lambda)$  and  $\Phi_{Spec}^n(k_{\parallel}, \lambda)$  are the spatial power density spectra of the diffused and specular component, respectively.  $\Phi_{Spec}^n(k_{\parallel}, \lambda)$  is updated at every iteration in order to account for the specular reflection properly with the relation

$$\Phi_{Spec}^n(k_{\parallel}, \lambda) = (1 - \alpha)\Theta^n(k_{\parallel}, \lambda), \quad (15)$$

$\alpha$  is the portion of incoming power that will be diffused, which in general can depend on  $\lambda$  and  $k_{\parallel}$ .  $\Theta^n(k_{\parallel}, \lambda)$  is the power contribution of plane waves with a certain  $k_{\parallel}$  value that are going to the bottom of the cell.  $\Theta^n(k_{\parallel}, \lambda)$  is calculated using

$$\Theta^1(k_{\parallel}, \lambda) = T_{first}(k_{\parallel}, \lambda), \quad (16)$$

in the first iteration and for the rest,

$$\Theta^n(k_{\parallel}, \lambda) = \sum_{k_{\parallel}'} P_{relaunch}^{n-1}(k_{\parallel}', \lambda) T_{k_{\parallel}'}(k_{\parallel}, \lambda). \quad (17)$$

Note that  $T_{first}(k_{\parallel}, \lambda)$  and  $T_{k_{\parallel}'}(k_{\parallel}, \lambda)$  give the complete information of how power is distributed to plane wave components propagating in the Si (towards -y). Thus, we can infer the values of  $A_{tot}(\lambda)$  and  $R_{tot}(\lambda)$  for any Si thickness of choice after simulating for a particular thickness, provided that the relaunch boundary is far enough from the top grating to avoid any possible near field effect.

From that information, we can calculate  $P_{Dif}^n(\lambda)$

$$P_{Dif}^n(\lambda) = \sum_{k_{\parallel}} \alpha \Theta^n(k_{\parallel}, \lambda), \quad (18)$$

where  $P_{Dif}^n(\lambda)$  is the total diffused power to be relaunched at iteration  $n$  which is then used to calculate  $\Phi_{Dif}^n(k_{\parallel}, \lambda)$  using

$$\Phi_{Dif}^n(k_{\parallel}, \lambda) = P_{Dif}^n(\lambda) \times F_{Dif}(k_{\parallel}), \quad (19)$$

$F_{Dif}(k_{\parallel})$  is the normalized spatial power density distribution of the wavefront coming out from the diffuser of our choice. For a Lambertian source,  $F_{Dif}(k_{\parallel}) = C_0 / (\sqrt{k^2 - k_{\parallel}^2})^{28,29}$  where  $C_0$  is a proportionality constant. One can infer the proper  $F_{Dif}(k_{\parallel})$  from radiant intensity measurements if one wishes to simulate for a realistic diffuser structure. Here, the back reflector is assumed to not couple light to any evanescent component. The iterative procedure is stopped when the total power to be relaunched  $P_{back}^n(\lambda)$  (towards +y) calculated with

$$\begin{aligned} P_{back}^n(\lambda) &= \sum_{k_{\parallel}'} \Theta^n(k_{\parallel}', \lambda) \\ &= \sum_{k_{\parallel}'} \sum_{k_{\parallel}} [P_{relaunch}^{n-1}(k_{\parallel}, \lambda) \times T_{k_{\parallel}}(k_{\parallel}', \lambda)], \end{aligned} \quad (20)$$

for  $n > 1$  reaches zero.

In the rest of this contribution, we only consider 2D systems, invariant along the z-axis. The full wave simulations here were done using the finite element method (COMSOL), however any tool can be employed. We only consider plane waves with Transverse Magnetic (TM) polarization (no out-of-plane electric field) for simplicity and clarity as the phenomena described below are not polarization specific. The diffraction efficiency of TE waves can be different than that of TM waves but the same phenomena discussed below occur for TE waves also. The specular reflection component of the back diffuser is assumed to be uniform for all wavelengths and angles of incidence, but a more thorough consideration can easily be implemented. For all wavelengths, we simulate the excitation of plane waves with a homogeneous grid  $\Delta k_{\parallel} = 0.025 \times k_{Si}$ . We then further interpolate the values of  $A_{k_{\parallel}}(\lambda)$ ,  $R_{k_{\parallel}}(\lambda)$  and  $T_{k_{\parallel}}(k_{\parallel}', \lambda)$  to a finer mesh with  $\Delta k_{\parallel} = 0.001 \times k_{Si}$ . We utilize relaunched  $k_{\parallel}$  cases in the range of  $-0.999 \times k_{Si} \leq k_{\parallel} \leq 0.999 \times k_{Si}$ . Due to symmetry of the front structures considered here, we only need to simulate for positive or negative values of  $k_{\parallel}$ .

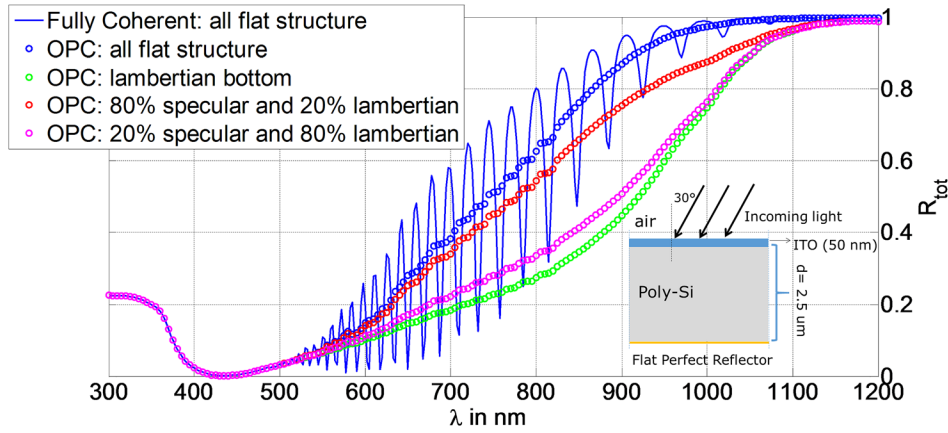


FIG. 3. Reflectance versus wavelength for flat top structures in the case of  $30^\circ$  incidence angle for different back reflectors. The inset shows the structure.

### III. BASIC EXAMPLES

As a first example, we show OPC calculations for a flat front surface with anti-reflection coating (50 nm indium tin oxide (ITO)), but with various back reflectors (Fig. 3). The light is incoming at an angle of  $30^\circ$  (arbitrary incidence angle is possible). The blue solid line shows the coherent calculation result for the reflectance, assuming a perfect flat mirror at the back of the cell which is modelled with a perfect electric conductor boundary. The resonances we see are Fabry-Perot type modes. The blue circles show the reflectance curve from partially coherent calculations for an all-flat structure (so with perfect specular reflection). We see that the partially coherent reflectance follows the average of the coherent case, as may be expected.

The green circle plot shows the reflectance when we assume a 100% Lambertian diffuser at the bottom. We see that there is a great decrease in reflectance due to the increased optical path length. The red and magenta circle plots show the in-between cases where there is partial specular reflection by the back diffuser, 20% and 80%, respectively. We see that in the presence of 20% specular reflection, its performance is still comparable to that of a Lambertian diffuser, an important point for choosing a functional back reflector.

For more complex examples, we simulate cells which have a grating at the front (see Fig. 1(a)) and various lossless diffusers without specular component at the back side. The grating geometry has period  $P = 400$  nm, fill-factor  $FF = 0.7$ , grating depth 300 nm, and ITO thickness 50 nm. The thickness of the Si layer is  $d = 2.5 \mu\text{m}$  (the same as in Fig. 3). We consider different back reflectors via the power density spectrum of the relaunched waves (Fig. 4(a)). This corresponds to different radiant intensity  $J(\alpha)$  in the far field (Fig. 4(b)) which can be calculated via the relation<sup>28,29</sup>

$$J(\alpha) = C \times F_{Dif}(k_{\parallel}) \cos^2(\alpha), \quad (21)$$

where  $C$  is a proportionality constant and  $\alpha$  is the angle with respect to the normal direction of the diffuser surface (thus  $k_{\parallel} = k \times \sin(\alpha)$ ). As mentioned before, all these different diffusers are modelled with the results of a single plane wave calculation sweep.

Fig. 5 demonstrates how one can further suppress reflection by combining a back diffuser with a grating patterned front. We plot the reflectance of several combined and back

diffuser only configurations with the three types of diffusers. For the structures with a flat front interface, there is a monotonous trend of  $R_{tot}(\lambda)$  reduction as we increase the diffusing capability of the rough diffuser (from a narrow distribution to Lambertian) as can be seen by comparing the dotted plots (Fig. 5). The combined structure with the Lambertian back diffuser (green solid line) still has the best performance compared with all the other structures. However, there is not much reduction in reflectance for the combined structure by increasing the spread of the back diffuser, unlike for the flat front interface structures.

We show later (Sec. V) how the enhancement of the combined structure will be more optimal with a larger Si thickness. In Sec. V, we further discuss how the performance

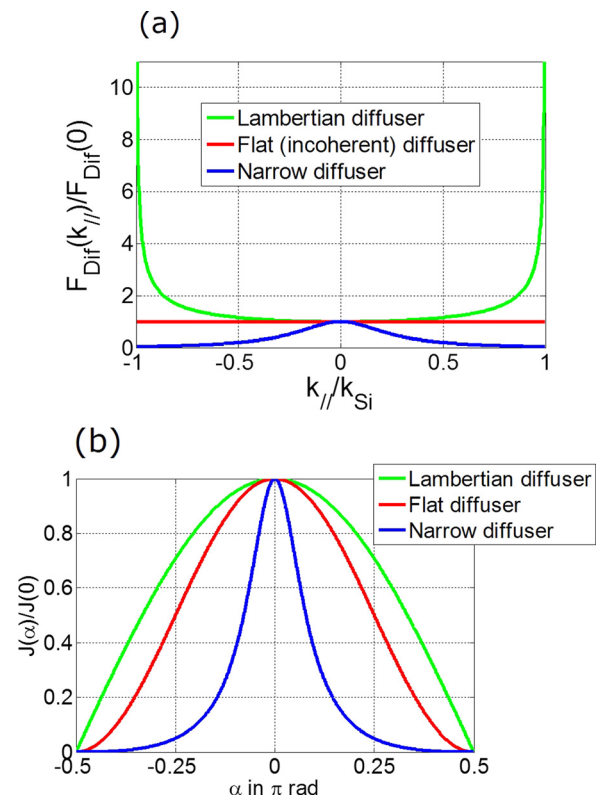


FIG. 4. (a) The spatial power density spectrum  $F_{Dif}(k_{\parallel})$  of the wavefront coming out of the diffuser. (b) The corresponding radiant intensity profiles.  $\alpha$  is the angle relative to the normal of the diffuser surface. The “narrow diffuser” radiant intensity has a Lorentzian shape with a linewidth of  $\pi/6$  rad.

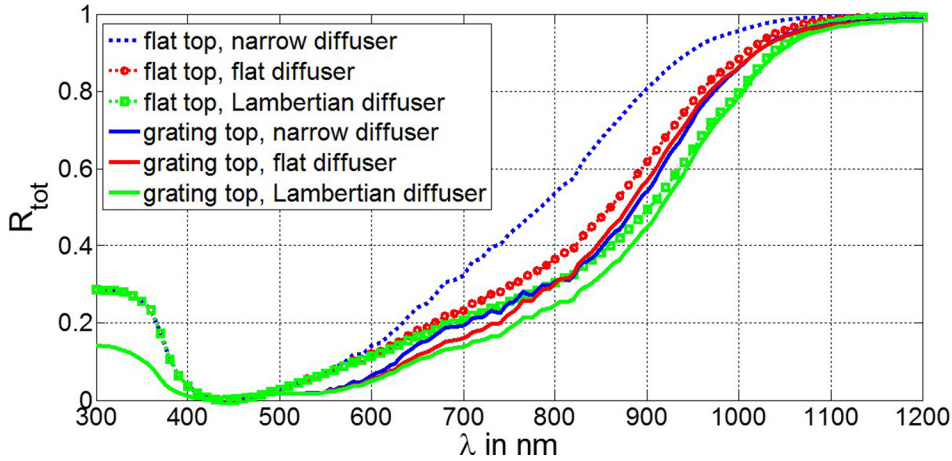


FIG. 5. Reflectance calculated with the OPC method of flat top (dotted curves) and grating top (solid curves) structure, for various types of diffusers.

of the combined structure depends on the specular reflection component, the Si thickness and the grating period.

The characteristics in Fig. 5 are explained by examining the escape transmittance of Si to air, thus the transmittance of the plane waves coming from the bottom (Fig. 1(b)). Fig. 6(a) gives this escape transmittance for a flat top structure. We see that beyond a certain  $k_{\parallel}$  (or angle), there is no more transmittance due to Total Internal Reflection (TIR). At shorter wavelengths, there is also no escape transmission due to the strong Si absorption. In the grating structure (Fig. 6(b)), we see that the escape transmittance for small  $k_{\parallel}$  is smaller. However, the TIR has been partially broken, as diffraction by the grating allows light at higher  $k_{\parallel}$  to escape to air. The dark triangle region of Fig. 6(b) in the wavelength range of 800–1200 nm and  $k_{\parallel}/k_{\text{Si}}$  range of

0.3–0.6 is the region where TIR is not broken and is determined by the grating periodicity.

The narrow diffuser works well with the grating structure because the diffuser redistributes the power to relatively low  $k_{\parallel}$  components, which have low escape transmission and thus give more light trapping effects. However, the gain of optical path length is still not as much as compared with a Lambertian diffuser.

There is less additional enhancement that is obtained when combining wide spread diffusers with a grating top, because they redistribute the power to high  $k_{\parallel}$  components. With the grating structure at the front surface, a substantial portion of the diffused light with high  $k_{\parallel}$  (range 0.4–0.6  $k_{\text{Si}}$ ) will have high escape transmittance. The reason why the Lambertian diffuser works better with the grating top (as compared with a flat diffuser) is because there is more power being distributed to very high  $k_{\parallel}$  ( $>0.8 k_{\text{Si}}$ ) components, which still have a low escape transmittance.

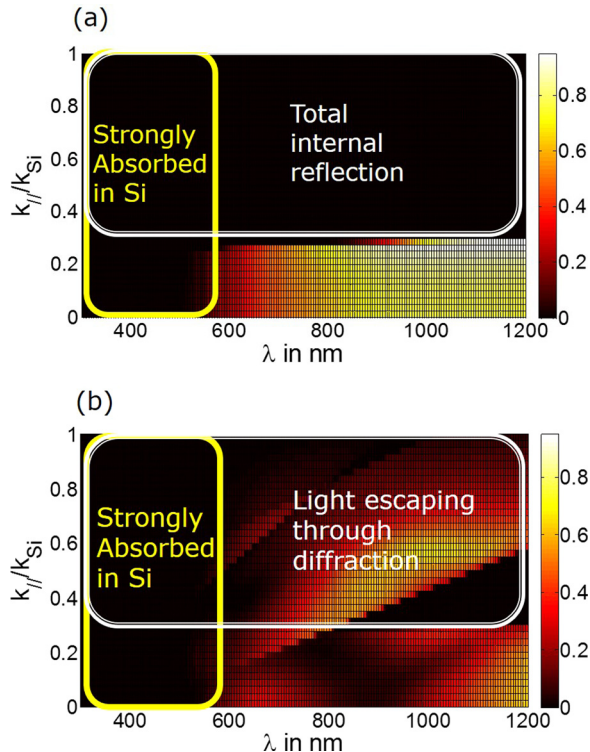


FIG. 6. Escape transmittance ( $R_{k_{\parallel}}(\lambda)$ ) of relaunched plane waves for (a) flat top structure ( $d = 2.5 \mu\text{m}$ ) and (b) grating top ( $P = 400 \text{ nm}$ ,  $d = 2.5 \mu\text{m}$ ). In all cases, the ITO thickness is 50 nm.

#### IV. IMPLICATIONS OF LIMITED COHERENCE ON ABSORPTION

Light coherence can influence absorption in a 1D multilayer solar cell structure.<sup>22,23</sup> Here, we show that having limited light coherence can improve absorption on average for a 2D solar cell structure over a fairly broad wavelength range when certain conditions are met. In Fig. 7, we compare the reflectance under fully coherent and OPC conditions for solar cell structures with the same top gratings and a (100%) specular bottom reflector. The geometric parameters of the grating are  $P = 400 \text{ nm}$ ,  $\text{FF} = 0.7$ , grating depth of 300 nm, and ITO thickness of 50 nm. The deviation of the OPC reflectance from the average reflectance under fully coherent conditions is less significant if the Si thickness is relatively small or large. For Si thickness 1  $\mu\text{m}$ , the OPC reflectance follows closely the average of coherent reflectance, as the OPC plot lies in between the peak and the dips of the coherent resonances. In contrast, the difference between OPC and average coherent is very apparent when  $d = 7.5 \mu\text{m}$ . This deviation again decreases for the thicker structures, e.g., when  $d = 30 \mu\text{m}$ .

When all the light at a certain wavelength is absorbed in a single pass, the total reflectance will converge to the first pass reflectance (the reflectance for infinite Si thickness). In

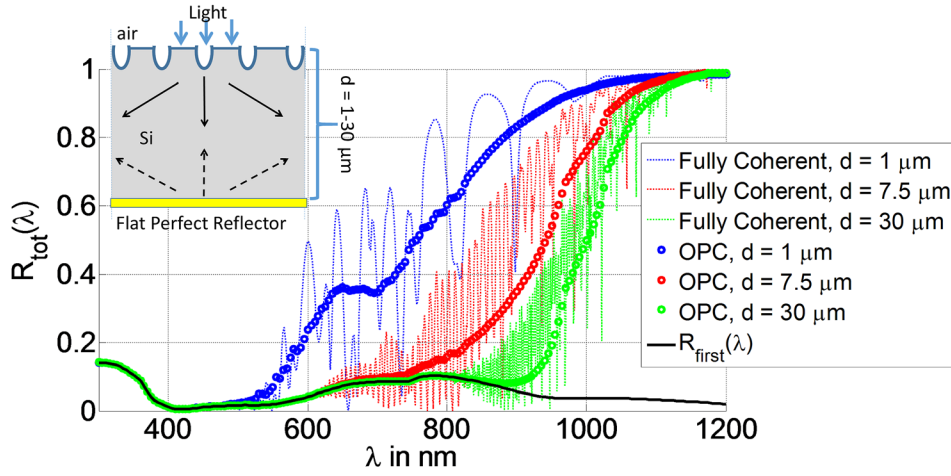


FIG. 7. Reflectance curves for the fully coherent and one pass coherent cases for top grating-flat bottom solar cell structures with different Si thicknesses. The top grating structure is the same as shown in Fig. 1(a) with  $P = 400$  nm.

this regime, the OPC and coherent case provide the same reflectance. The particular wavelength edge, where interplay between front and back interface becomes important, depends on the Si thickness (around 550 nm for  $d = 1 \mu\text{m}$ , 900 nm for  $d = 30 \mu\text{m}$ ).

The dependence of absorption on light coherence stems from the constructive phase relation necessary for waveguide modes. This phase restriction makes diffraction of fully coherent light efficient only at specific  $k_{\parallel}$  values and wavelengths. This condition is relaxed if most of the light coming back from the bottom has been absorbed substantially in one pass or when coherence is lost, as in the OPC calculations. For incoherent waves, diffraction to high  $k_{\parallel}$  values in the regime of TIR does not need to fulfil any phase relation and thus it will always be an allowed process. However, if the material absorption is too weak or if the optical path length is only slightly increased by diffraction, the absorption enhancement is reduced. In other words, the absorption of the diffracted waves cannot be too strong or too weak in order to see this effect. Thus, it is typically apparent at longer wavelengths (around 800–1000 nm for Si), when light travels multiple passes in the active layer and certain geometrical conditions are fulfilled.

Fig. 7 demonstrates this analysis. Note that the optical path length gain by scattering light to higher  $k_{\parallel}$  is proportional to the thickness  $d$ . At small thickness ( $d = 1 \mu\text{m}$ ), there is not much gain in optical path length by coupling to waveguide modes. For  $d = 30 \mu\text{m}$ , a significant portion of the diffracted waves would already be absorbed in a single pass and thus there is weaker OPC reflectance deviation from the fully coherent average. For the in-between thickness of  $d = 7.5 \mu\text{m}$ , light at longer wavelengths is not over-absorbed in just a single pass and there is significant increase in optical path length upon diffraction. Thus, incoherence has a significant influence on absorption at  $d = 7.5 \mu\text{m}$ . This explains why there is stronger deviation from the fully coherent average.

To quantify, we calculate a figure of merit in the wavelength region of 750–1200 nm

$$\gamma = (WIR_{FC} - WIR_{OPC})_{750-1200\text{nm}}, \quad (22)$$

where  $WIR$  is the weighted integrated reflection of the AM1.5G solar spectrum which is defined as

$$WIR = \frac{\int R_{Tot}(\lambda) \times P_{AM1.5G}(\lambda) d\lambda}{\int P_{AM1.5G}(\lambda) d\lambda}, \quad (23)$$

$P_{AM1.5G}(\lambda)$  is the power spectrum of the AM1.5G solar radiation. The subscript FC and OPC refers to the fully coherent and OPC condition, respectively. We choose this wavelength regime for Si cells, as the effect of limited coherence (and all light-trapping features) should be apparent there.

We plot  $\gamma$  as a function of Si thickness in Fig. 8, and see that there is an optimal thickness, as the previous analysis predicts. The solar cell structure with  $d = 7.5 \mu\text{m}$  has around 9% less reflectance when incoming light has limited coherence. When Si thickness is further increased, the difference in  $WIR$  approaches the initial value for the very thin thickness  $d = 1 \mu\text{m}$ . We also note that the fully coherent  $WIR$  is larger than the OPC  $WIR$  even at  $d = 1 \mu\text{m}$ , where the OPC reflectance is close to the fully coherent average. This is due to the AM1.5G power spectrum and the nature of the Fabry-Perot resonances, which have a free spectral range (FSR) proportional to the square of the wavelength and inversely proportional to the thickness. The FSR will increase more rapidly at thin thicknesses as the wavelength increases, providing for less reflectance dips in the wavelength region of interest (Fig. 7, coherent case for  $d = 1 \mu\text{m}$ ).

As the effect of coherence depends on the absorption of the diffracted waves, we therefore expect that it is affected by the periodicity of the grating. We compare in Fig. 9 the reflectance of structures with a flat bottom and a grating top for  $P = 1000$  nm and  $P = 400$  nm with  $d = 2.5 \mu\text{m}$  and  $7.5 \mu\text{m}$ .

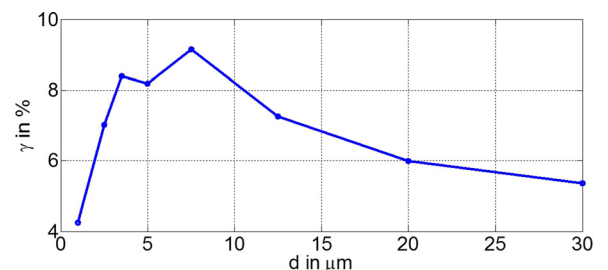


FIG. 8. Plot of  $\gamma$  versus Si thickness  $d$  for the structure of Fig. 7.

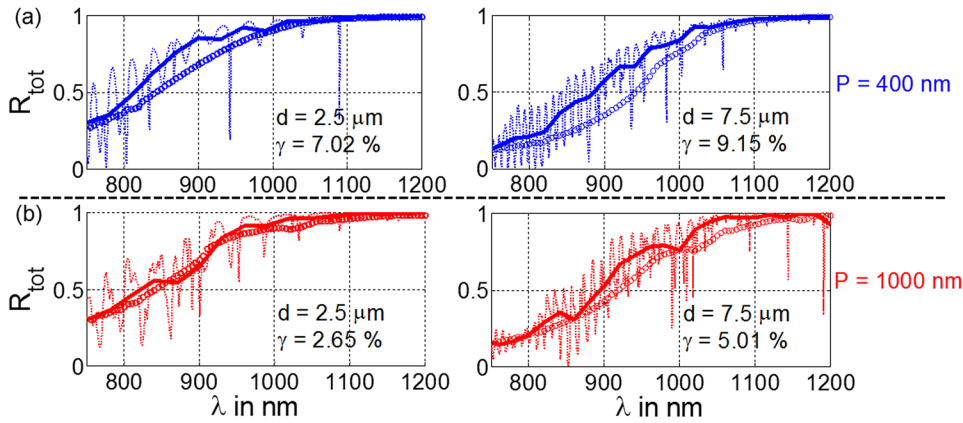


FIG. 9. Comparing the fully coherent and OPC case for (a)  $P=400$  nm with  $d=2.5\ \mu\text{m}$  and  $d=7.5\ \mu\text{m}$ , and for (b)  $P=1000$  nm with  $d=2.5\ \mu\text{m}$  and  $d=7.5\ \mu\text{m}$ . For all structures, the bottom reflector is 100% specular,  $FF=0.7$  and grating depth of 300 nm. The dotted line plots are the reflectance for the fully coherent case. The solid line plots are the average reflectance of the fully coherent case, with wavelength averaging window 20 nm. The circle plots are the reflectance for the OPC case.

Comparing Fig. 9(a) with 9(b), we see that the OPC case reflectance deviates more from the fully coherent average reflectance for lower periodicities. The fact that the  $\gamma$  values for  $P=1000$  nm are significantly lower than for  $P=400$  nm further demonstrates that the effect of limited coherence is weaker at larger grating periodicities. This is because the larger period couples to less oblique angles, which leads to less influence of guided modes and their phase restrictions. In other words, the absorption of the diffracted waves when  $P=1000$  nm is too low to make much difference as compared with when  $P=400$  nm for the two Si thickness cases.

## V. OPTIMAL COMBINED STRUCTURE

It is of great interest to investigate the effect of specular reflection (Sec. VA), Si thickness (Sec. VB) and front grating periodicity (Sec. VC) in combined devices. Obtaining a perfect Lambertian diffuser is not always feasible and one would wish to see how much specular reflection is acceptable. When considering the thickness of the active material, there is a trade-off that comes into play. The gain of a Lambertian diffuser would not be apparent when the active material is too thin, as the optical path length is not that long upon deviation. On the other hand, if the active material is too thick, most of the light will already be absorbed before reaching the diffuser. The grating periodicity basically controls the escape transmittance of the diffused light with high  $k_{\parallel}$ , while also influencing the first pass reflection. Thus, one would expect there is an optimal periodicity that maximizes the benefit of the combined structure.

## A. Specular reflection

The absorption enhancement by just having a front grating structure (with a perfect specular reflector at the back) is already significant. Fig. 10 shows results for a combined diffuser-grating system with  $d=2.5\ \mu\text{m}$ , assuming a lossless back Lambertian diffuser with 100%, 50%, and 0% specular component, respectively. The blue line curve is for fully coherent simulations with a 100% specular back reflector, the blue circles give the reflectance under OPC conditions. Comparing both of these blue plots with the black dashed curve (which gives the OPC reflectance of an all flat structure without grating), we see that there is much reduction in reflectance just by introducing the top grating structure. Indeed, the top grating structure gives both better antireflection properties and improves the optical path length inside the Si.

Combining the front gratings with a back diffusing element can further enhance the absorption, even in the presence of significant specular reflection at the back diffuser. This can be seen by comparing the red squared and green dashed-dot plot (Fig. 10), which show the reflectance of the combined structure with a 50% specular and 50% Lambertian back diffuser and with perfect Lambertian diffuser (0% specular), respectively. The reflectance for these two structures is comparable, although the combined structure with fully Lambertian back diffuser still performs better. There is significant reduction in reflectance by more than 10% in the wavelength range of 800–1000 nm for the combined structures. With the perfect Lambertian back reflector,

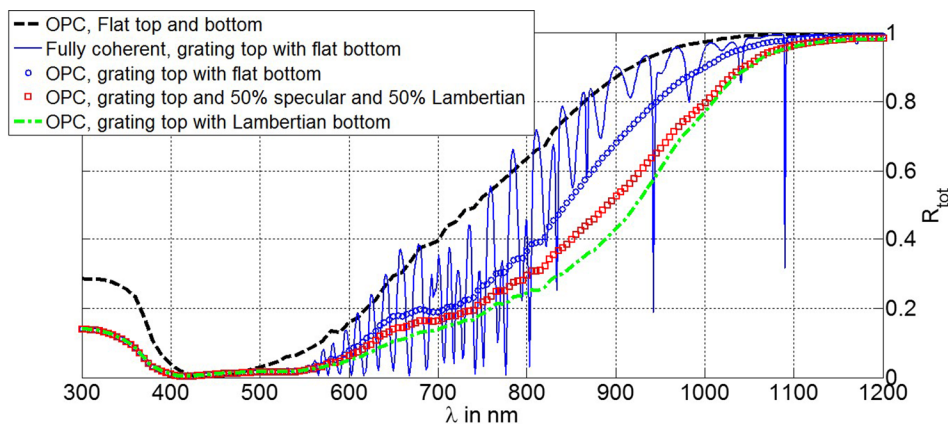


FIG. 10. Total reflectance of combined diffuser-grating structure ( $P=400$  nm,  $d=2.5\ \mu\text{m}$ ) assuming different specular components for the diffuser. For comparison, the reflectance of an all flat structure without any front grating and back diffuser under OPC condition is the black dashed line. The geometrical parameters of the top grating are  $P=400$  nm,  $FF=0.7$ , grating depth of 300 nm, and ITO thickness of 50 nm.

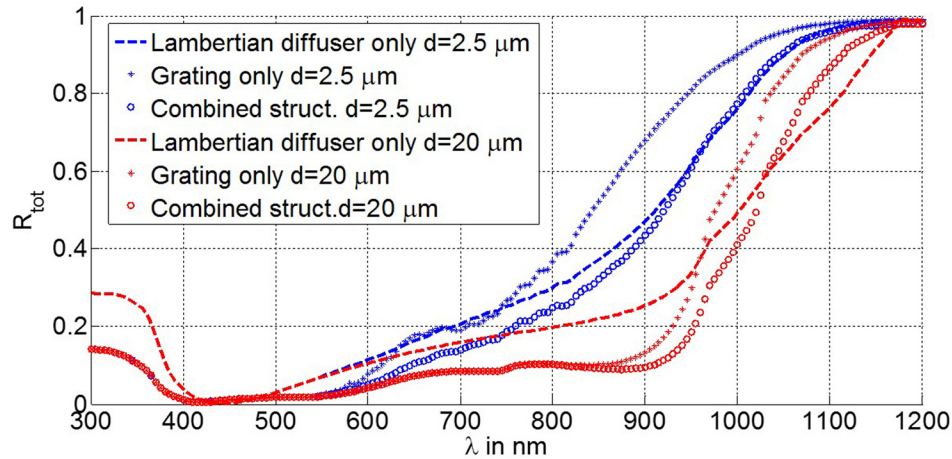


FIG. 11. Total reflectance of combined diffuser-grating structures and single element structures. The geometrical parameters of the top gratings are the same as in Fig. 10.

the reflectance reduction can be more than 20% in this wavelength range.

The flat top and perfect specular bottom structure has a *WIR* of 38.5%. The front patterned only configuration has 27.9%, and the Lambertian back diffuser only configuration has 26.5%. Finally, the combined Lambertian back diffuser-front grating configuration has a *WIR* down to 22.2%.

## B. Si thickness

There is an optimum Si thickness at which the advantage of having a combined back diffuser and front grating structure is maximized. This can be seen in Fig. 11 which shows the reflectance of single-element and combined structures under the OPC condition for two different Si thicknesses  $d$ . For both  $d$  values, the combined structure outperforms the single element structures. At larger  $d = 20 \mu\text{m}$ , the combined structure has significantly lower reflectance than the Lambertian back diffuser only configuration, more so than for  $d = 2.5 \mu\text{m}$ . This is because there is more increase in optical path length by scattering light to oblique angles when  $d$  is larger. Thus, the Lambertian back diffuser can significantly improve the absorption of light only when  $d$  is large enough. However, at large  $d$  values, a significant portion of light is absorbed in the first pass and leaves smaller room for improvement via the Lambertian diffuser, except in the longer wavelength range. This is the reason why the reflectance of the combined structure is close to the grating only configuration in the wavelength range  $< 850 \text{ nm}$  at  $d = 20 \mu\text{m}$  (red star and circle plots).

It is also seen in Fig. 11 that the Lambertian diffuser only reflectance curve crosses the other curves at certain wavelengths, which indicates a change of the dominant absorption mechanism. The crossing between the Lambertian diffuser only and grating only reflectance curves indicates the start of the longer wavelength regime where first pass absorption is no longer dominant. The crossing between the Lambertian diffuser only and combined configuration curves indicates the start of the longer wavelength regime where absorption is mainly determined by the escape transmittance ( $R_{k_{||}}(\lambda)$ ).

The *WIR* versus  $d$  plot in Fig. 12(a) confirms that the performance of a front grating only configuration becomes close to the combined structure above a certain Si thickness. The *WIR* difference between the front grating only configuration

and the combined structure is less than 3% for  $d > 10 \mu\text{m}$ . Even so, the combined structure has in general less reflectance than single element structures.

The effect of specular reflection at the back also becomes less important as  $d$  becomes larger. Fig. 12(b) shows the *WIR* as a function of the bottom specular reflection percentage for various Si thicknesses of the combined structure. The difference in *WIR* between a 100% specular back reflector and Lambertian back diffuser is also less than 3% for  $d > 10 \mu\text{m}$ .

## C. Grating periodicity

The effect of front grating periodicity can be surprisingly weak for the combined grating-top-Lambertian-bottom structures in the top periodicity range of 300–1000 nm. Reflectance for different front grating periodicities, but with identical fill factor and grating depth, is shown in Fig. 13 for Si thickness  $d = 7.5 \mu\text{m}$ . The similarity between these

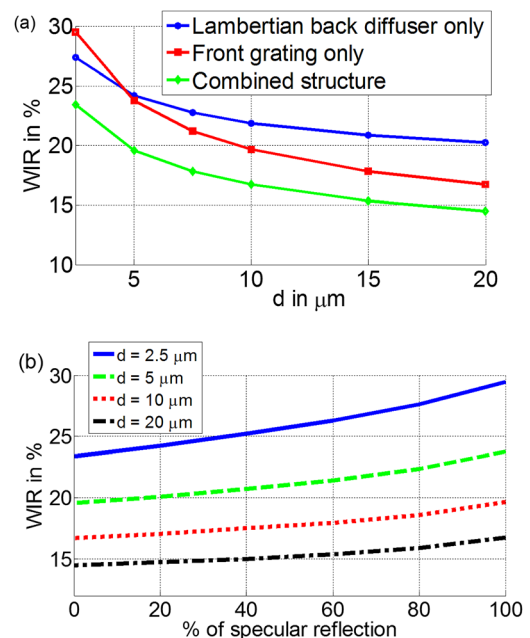


FIG. 12. (a) *WIR* versus Si thickness. (b) *WIR* versus % of specular reflection at different Si thicknesses for the combined structure.

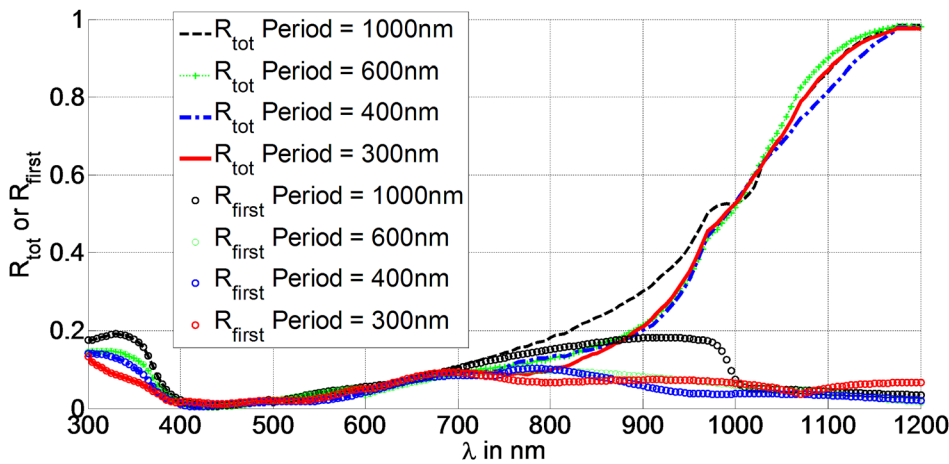


FIG. 13. Total and first-pass reflectance of combined structures with front gratings and Lambertian back diffuser for several different grating periods. The gratings have fill factor 0.7 and grating depth 300 nm. The Si thickness is  $d = 7.5 \mu\text{m}$  and the ITO thickness is 50 nm.

gratings is connected to the fact that they have comparable first-pass reflectance. In addition, the escape transmittance of waves with high  $k_{\parallel}$  is similar in a broad wavelength range for these structures (not shown). This is relevant here as high  $k_{\parallel}$  components are dominant for a Lambertian diffuser (Fig. 4(a)). The combined structure with front grating period  $P = 1000 \text{ nm}$  is significantly more reflecting (around 10%) in the wavelength region of 750–950 nm compared with the other systems. This is mainly due to the slightly larger first pass reflectance for  $P = 1000 \text{ nm}$  in that wavelength range. For thinner Si thickness  $d$ , the difference in reflectance between these structures becomes less apparent.

## VI. CONCLUSION

A calculation method to efficiently address structures that couple wave and ray optics is discussed. The OPC calculations take wave effects into account where they matter the most, while evading a large computational domain to model rough structures. A general rough diffuser is handled directly via the reflected wavefront, instead of its geometry. A single plane wave calculation sweep provides all the information to calculate any kind of bottom diffuser.

We utilize the calculation method to study solar cell structures which combine gratings at the front and a rough diffuser at the back, which has been realized in state-of-the-art thin film Si devices.<sup>30</sup> Results clearly show that the combined structures provide more light trapping capabilities than single element devices. We elucidate the important dependence on the active material thickness and the specular reflection component of the bottom diffuser.

We demonstrate that partially coherent light can be more efficiently absorbed than fully coherent light over a fairly broad wavelength range for an important range of Si thicknesses. This phenomenon is due to the existence of an additional phase condition that is imposed on the waves diffracted in the fully coherent case. Therefore, the back reflector in advanced thin-film devices needs careful consideration.

## ACKNOWLEDGMENTS

This work is supported by the Flemish IWT-SBO project SiLaSol (Number 3E100243) and the Interuniversity Attraction

Poles program of the Belgian Science Policy Office under Grant No. IAP P7-35 “*photonics@be.*” The authors wish to thank Emiliano Rezende Martins, Ounsi El Daif, and Tigran Baghdasaryan for helpful discussions. Sven Leyre would like to thank the SIM (Flemish Strategic Initiative for Materials) and IWT (Flemish agency for Innovation by Science and Technology) for their financial support through the SoPPoM project within the SIBO program.

<sup>1</sup>C. Trompoukis, O. El Daif, V. Depauw, I. Gordon, and J. Poortmans, *Appl. Phys. Lett.* **101**, 103901 (2012).

<sup>2</sup>A. Abass, H. Shen, P. Bienstman, and B. Maes, *J. Appl. Phys.* **109**, 023111 (2011).

<sup>3</sup>A. Bozzola, M. Liscidini, and L. C. Andreani, *Opt. Express* **20**, A224 (2012).

<sup>4</sup>K. Q. Le, A. Abass, B. Maes, P. Bienstman, and A. Alù, *Opt. Express* **20**, A39 (2012).

<sup>5</sup>K. Jager, M. Fischer, R. A. C. M. M. van Swaaij, and M. Zeman, *J. Appl. Phys.* **111**, 083108 (2012).

<sup>6</sup>M. Schulte, K. Bittkau, K. Jager, M. Ermes, M. Zeman, and B. E. Pieters, *Appl. Phys. Lett.* **99**, 111107 (2011).

<sup>7</sup>S. Fahr, T. Kirchartz, C. Rockstuhl, and F. Lederer, *Opt. Express* **19**, A865 (2011).

<sup>8</sup>S. Fahr, C. Rockstuhl, and F. Lederer, *Appl. Phys. Lett.* **92**, 171114 (2008).

<sup>9</sup>P. Kowalczewski, M. Liscidini, and L. C. Andreani, *Opt. Lett.* **37**, 4868 (2012).

<sup>10</sup>O. El Daif, E. Drouard, G. Gomard, A. Kaminski, A. Fave, M. Lemiti, S. Ahn, S. Kim, P. Roca i Cabarrocas, H. Jeon, and C. Seassal, *Opt. Express* **18**, A293 (2010).

<sup>11</sup>X. Meng, V. Depauw, G. Gomard, O. El Daif, C. Trompoukis, E. Drouard, C. Jamois, A. Fave, F. Dross, I. Gordon, and C. Seassal, *Opt. Express* **20**, A465 (2012).

<sup>12</sup>S. Mookapati, F. J. Beck, A. Polman, and K. R. Catchpole, *Appl. Phys. Lett.* **95**, 053115 (2009).

<sup>13</sup>Z. Yu, A. Raman, and S. Fan, *Opt. Express* **18**, A366 (2010).

<sup>14</sup>C. Battaglia, C.-M. Hsu, K. Söderström, J. Escarré, F.-J. Haug, M. Charrière, M. Boccard, M. Despeisse, D. T. L. Alexander, M. Cantoni, Y. Cui, and C. Ballif, *ACS Nano* **6**, 2790 (2012).

<sup>15</sup>P. N. Saeta, V. E. Ferry, D. Pacifici, J. N. Munday, and H. A. Atwater, *Opt. Express* **17**, 20975 (2009).

<sup>16</sup>P. Spinelli, M. A. Verschuuren, and A. Polman, *Nat. Commun.* **3**, 692 (2012).

<sup>17</sup>H. Shen and B. Maes, *Opt. Express* **19**, A1202 (2011).

<sup>18</sup>A. Abass, K. Q. Le, A. Alù, M. Burgelman, and B. Maes, *Phys. Rev. B* **85**, 115449 (2012).

<sup>19</sup>V. E. Ferry, A. Polman, and H. A. Atwater, *ACS Nano* **5**, 10055 (2011).

<sup>20</sup>D. Madzharov, R. Dewan, and D. Knipp, *Opt. Express* **19**, A95 (2011).

<sup>21</sup>E. R. Martins, J. Li, Y. Liu, J. Zhou, and T. F. Krauss, *Phys. Rev. B* **86**, 041404 (2012).

<sup>22</sup>R. Santbergen, A. H. M. Smets, and M. Zeman, *Opt. Express* **21**, A262 (2013).

- <sup>23</sup>M. C. Tropicovsky, A. S. Sabau, A. R. Lupini, and Z. Zhang, *Opt. Express* **18**, 24715 (2010).
- <sup>24</sup>C. C. Katsidis and D. I. Siapkas, *Appl. Opt.* **41**, 3978 (2002).
- <sup>25</sup>E. Centurioni, *Appl. Opt.* **44**, 7532 (2005).
- <sup>26</sup>J. S. C. Prentice, *J. Phys. D* **33**, 3139 (2000).
- <sup>27</sup>W. Lee, S.-Y. Lee, J. Kim, S. C. Kim, and B. Lee, *Opt. Express* **20**, A941 (2012).
- <sup>28</sup>A. Starikov and A. T. Friberg, *Appl. Opt.* **23**, 4261 (1984).
- <sup>29</sup>W. H. Carter and E. Wolf, *J. Opt. Soc. Am.* **65**, 1067 (1975).
- <sup>30</sup>C. Trompoukis, A. Herman, O. El Daif, V. Depauw, D. Van Gestel, K. Van Nieuwenhuysen, I. Gordon, O. Deparis, and J. Poortmans, in *Enhanced Absorption in Thin Crystalline Silicon Films for Solar Cells by Nanoimprint Lithography*, Photonics for Solar Energy Systems IV (SPIE, Brussels, Belgium, 2012).